applied optics

Experimental demonstration and optimization of X-ray StaticCodeCT

Angela P. Cuadros,[1,*] **Xiaokang Liu,**[1] **Paul E. Parsons,**[1] **Xu Ma,**[2] **and Gonzalo R. Arce**[1]

[1]*Department of Electrical and Computer Engineering, University of Delaware, Newark, Delaware 19716, USA*
[2]*Key Laboratory of Photoelectronic Imaging Technology and System of Ministry of Education of China, School of Optics and Photonics, Beijing Institute of Technology, Beijing 100081, China*
Corresponding author: cuadrosa@udel.edu

As the use of X-ray computed tomography (CT) grows in medical diagnosis, so does the concern for the harm a radiation dose can cause and the biological risks it represents. StaticCodeCT is a new low-dose imaging architecture that uses a single-static coded aperture (CA) in a CT gantry. It exploits the highly correlated data in the projection domain to estimate the unobserved measurements on the detector. We previously analyzed the StaticCodeCT system by emulating the effect of the coded mask on experimental CT data. In contrast, this manuscript presents test-bed reconstructions using an experimental cone-beam X-ray CT system with a CA holder. We analyzed the reconstruction quality using three different techniques to manufacture the CAs: metal additive manufacturing, cold casting, and ceramic additive manufacturing. Furthermore, we propose an optimization method to design the CA pattern based on the algorithm developed for the measurement estimation. The obtained results point to the possibility of the real deployment of StaticCodeCT systems in practice.   © 2021 Optical Society of America

1. INTRODUCTION

Given the various computed tomography (CT) scanning technologies available today, multiple approaches to reduce X-ray radiation dosage while preserving reconstruction quality for imaging analysis have been recently proposed [1]. Coded aperture X-ray CT (CAXCT) is one state-of-the-art method that typically requires the use of tens to hundreds of different coded aperture (CA) patterns in a single scan to attain satisfactory image reconstruction quality. Furthermore, the physical CA has to be changed in concert with the view angles, making its implementation impractical [2]. In contrast, we recently introduced a radically new approach to CAXCT that uses a single-static CA in the CT gantry, together with a new method for image reconstruction tailor-made for the new sensing mechanism coined StaticCodeCT [3]. We showed that the 3D tensor formed by stacking the 2D coded CT projections of StaticCodeCT is low-rank. Additionally, we showed that the correlation of the multidimensional data can be efficiently exploited to synthesize the missing measurements, allowing fast and accurate 3D object recovery using standard CT reconstruction algorithms, particularly the Feldkamp-Davis-Kress (FDK) algorithm.

Given the StaticCodeCT architecture, a fundamental question arises: Can we design the structure of the CA to maximize the quality of image reconstruction and, if so, how? Our previous work has addressed the mask optimization problem in

CAXCT based on the structure of the sensing matrix [4–6]. Specifically, because the sensing matrices in CT are sparse and structured, we demonstrated that random CAs are suboptimal and that, by optimizing the binary pattern of the Cas, we can attain higher reconstruction quality [7,8]. Here, however, we cannot apply the same methods because they are tailor-made for iterative reconstruction approaches under the umbrella of compressive sensing (CS). Tensor completion relies on different mathematical principles; thus, the code aperture optimization in StaticCodeCT is still an open problem. This manuscript develops an optimization framework based on the data completion strategy used to estimate the missing data that we presented in [3]. Details on the CA optimization algorithm are provided in Section 3.

To attain structured illumination in transmission X-ray imaging, materials with high attenuation factors, or high densities, are inserted in the paths of the X-ray beams. Machining of high-Z alloys, for instance, was used by Holmgren *et al.* to manufacture CAs in [9]; however, this technique requires special design considerations given the limitations of the machines and materials involved in the process. To address these constraints, the authors proposed a more flexible approach based on conventional 3D printing. Specifically, they 3D printed the CA patterns in plastic, filled them with tungsten powder, and sealed them with epoxy. Nonetheless, for high-resolution

CAs, it is challenging to accurately fill the holes and clean the elements of the structure through which the X-rays must pass. Recently, other manufacturing techniques have been used to construct X-ray collimators, as well as CAs such as metal additive manufacturing [10], cold-casting [11], and ceramic additive manufacturing [12]. Yet, to the best of the authors' knowledge, none of these methods have been used to build CAs for use in X-ray transmission CT. The contributions of this work are thus twofold. First, we developed a CA optimization algorithm that builds upon the principles of the algorithms used for the tensorial completion of measurements. Second, we present a test-bed implementation of the StaticCodeCT system using three manufacturing techniques for CA prototyping. We demonstrate that using low-cost manufacturing methods, such as 3D printing with cold casting, together with the proposed CA optimization, we can reconstruct a 3D object with high accuracy. Using a microtomography cone-beam CT system, we attained reconstructions with peak signal-to-noise ratios (PSNR) of up to 32 dB while reducing 70% of the full-scan radiation dosage.

2. FORWARD MODEL

StaticCodeCT for a cone-beam system uses a single 2D CA pattern, which is static with respect to the CT gantry. As shown in Fig. 1, this system is mechanically simple and can thus be readily implemented on existing scanners. For the depicted cone-beam X-ray CT system, the source location varies continuously in a circular trajectory around the object, and the X-ray projections $I(E)$ are measured at different angles using a 2D flat panel detector (FPD). The projections are given by Beer–Lambert's law [13]:

$$I(E) = S(E)\,T(E)\,Q(E)\,P(E)\,\exp\left(-\int_\ell \mu(\ell, E)\mathrm{d}\ell\right),$$
(1)

where $\mu(\ell, E)$ is the linear attenuation coefficient of the object at position ℓ, $S(E)$ is the X-ray source spectrum, $Q(E)$ is the energy-dependent detector response, $T(E)$ accounts for the effect of the CA, and $P(E)$ is the effective energy flux. Namely, $T(E) = \exp[-\mu_b(E)\delta]$, where $\mu_b(E)$ is the linear attenuation coefficient of the blocking element at the energy E, and δ is the length of the intersection of the X-ray beam with the CA blocking element. In the ideal case, $T(E) \approx 0$ for the blocking elements; otherwise, $T(E) \approx 1$. In this paper, this approximation is valid for the testbed experiments given the thresholding algorithm applied to the measurements before reconstruction, as detailed in Section 4.

After discretizing the system, the projections at the $M_1 \times M_2$ 2D FPD can be rewritten as follows:

$$\mathbf{y} = \mathbf{CHx},$$
(2)

where $\boldsymbol{x} \in \mathbb{R}^{N^3}$ is a column vector corresponding to the linear attenuation coefficients of the $N \times N \times N$ object under inspection, $\boldsymbol{H} \in \mathbb{R}^{M_1 M_2 P \times N^3}$ is the system matrix, where each value $\mathbf{H}_{ji}$ in the matrix corresponds to the intersection length of ray j with voxel i, and $\boldsymbol{C} \in \mathbb{R}^{D \times M_1 M_2 P}$ is a binary matrix that accounts for the CA, where D is the number of unblocked elements in the system. Particularly, in the column vectors of
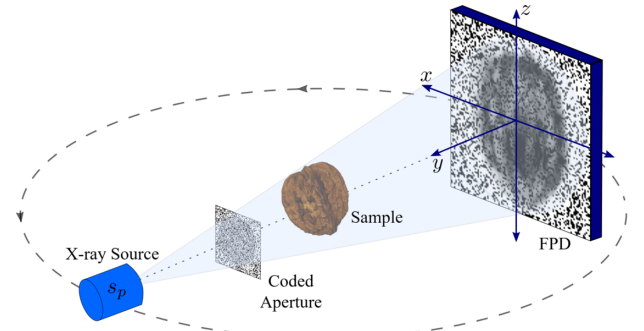

Fig. 1. StaticCodeCT system in a cone-beam setting. A static CA mask is placed in front of the rotating source.

$\mathbf{C}$, $\boldsymbol{c}_j \in \mathbb{R}^D = 0$ if the jth detector element corresponds to a blocking CA element. The remaining column vectors form the standard basis in $\mathbb{R}^D$. Conventionally, the linear attenuation coefficients, $\mathbf{x}$, are recovered by solving the following regularization problem in CAXT [2]:

$$\hat{\mathbf{x}} = \underset{\mathbf{x}}{\arg\min}\,\|\mathbf{y} - \mathbf{CHx}\|_2^2 + \lambda\Phi(\mathbf{x}),$$
(3)

where λ is a regularization constant, $\|\cdot\|_2$ corresponds to the ℓ_2 norm, and $\Phi(\mathbf{x})$ represents any prior information about the data. In CAXCT, this term usually promotes the sparsity of the object on a particular basis; then, conventional CS algorithms are used to solve the ill-posed inverse problem [14]. In contrast, we proposed a novel two-step reconstruction framework to reconstruct the 3D object in [3], which exploited the correlation in the measurement space rather than using prior information about the object data. Specifically, we first construct a 3D tensor of observations by stacking the 2D FPD measurements; then, we formulate a tensor completion problem in the measurement domain as follows:

$$\hat{\mathcal{S}} = \underset{\mathcal{S}}{\arg\min}\,\mathrm{rank}\,(\mathcal{S})\;\text{s.t.}\;\mathcal{P}_\Omega\,(\mathcal{S}) = \mathcal{P}_\Omega\,(\mathcal{Y}),$$
(4)

where $\hat{\mathcal{S}}$ is the estimate of the projection data tensor, $\mathcal{Y}$ is the observed incomplete tensor, and $\mathcal{P}_\Omega(\mathcal{Y}) = \mathcal{Y}(i, j, k)$ for $(i, j, k) \in \Omega$; otherwise, $\mathcal{P}_\Omega(\mathcal{Y}) = 0$, and Ω is the index set of the detector elements associated with the unblocking CA elements. In this paper, we used the algorithm described in [3] to estimate the missing measurements at the FPD by exploiting the low-rank nature of the 3D tensor as described in Eq. (4). Then, given the synthesized full set of cone-beam measurements, the physics governing the X-ray projection measurements are used to accurately recover the 3D object using the FDK or iterative image reconstruction algorithms.

3. CA OPTIMIZATION

The CAs elements in X-ray transmission can take two values: 0 to block the X-ray beam (opaque region) or 1 to let the X-ray beam pass (transparent region). The correct design and distribution of the elements in the CA can have an impact on the reconstruction quality. Interestingly, in [2], Kaganovsky *et al.* showed that randomly subsampling the detectors at each view angle exhibited the reconstructions with the lowest error.

However, because the sensing matrices in CT are sparse and structured, due to the nature of line-integral projections, random CAs are suboptimal according to CS theory [4,15]. Several strategies taken for the design of CAs have shown that better than random distributions can be found to produce reconstructions of higher quality. For example, in [7], Cuadros *et al.* proposed an optimization approach to design the structure of the CAs based on the minimization of the coherence of the sensing matrix for fan-beam CT. Then, to accelerate the optimization, similar efforts using a different cost function based on the mutual information of the sensing matrix were proposed in [5,6]. However, all of these methods generate different CA patterns for each view angle, which is not feasible in real applications. Furthermore, they are tailor-made for iterative reconstruction approaches that minimize cost functions with sparse regularizations under the CS framework. In contrast, the reconstruction algorithm developed in [3] relies on different mathematical principles; thus, the optimization of the CAs is still an open problem.

As described in [3], the initialization for the tensor of measurements is based on the matrix completion of the individual frontal slices corresponding to the FPD measurements at each angle. Mathematically, the problem is to recover the original set of measurements $\mathcal{S}^p$ from the observed measurements $\mathbf{Q}^{(p)} = \mathcal{P}_\Omega(\mathcal{S}^p) + V = \mathcal{P}_\Omega(\mathcal{Y}^p)$, where V is additive white Gaussian noise with standard deviation σ. The estimated FPD measurements at each pth view angle are then estimated as follows:

$$\hat{\mathcal{S}}^p = \underset{\mathcal{S}^p}{\mathrm{argmin}}\ \frac{1}{2\sigma^2}\|\mathbf{Q}^{(p)} - \mathcal{P}_\Omega\left(\mathcal{S}^p\right)\|_2^2 + \lambda\,\Phi\left(\mathcal{S}^p\right), \quad \textbf{(5)}$$

where $\Phi(\mathcal{S})$ is a regularization term. The matrix completion problem is to recover an $M_1 \times M_2$ frontal slice of the measurements' tensor when only $m \ll M_1 M_2$ of its entries are observed. Thus, in this work, the goal is to find the location of the m nonzero entries on the CAs, such that higher-quality estimations are obtained when using the matrix completion framework. Matrix completion can recover an $M \times M$ matrix of low-rank r from $Mr\log_2 M$ noisy randomized samples with an error proportional to the noise level. If the missing entries are spread across the rows of the matrix, even fewer matrix observations are needed for recovery [16]. Pimentel-Alarcon *et al.* showed that uniform sampling of the matrix with only $\max(r, \log_2 M)$ observed entries per column satisfies recovery conditions with high probability [17]. As described in [3], the estimation of the FPD measurements is similar to an image inpainting problem solved using matrix completion algorithms during initialization. Thus, we optimize the CA pattern such that the passing elements are as uniformly spread as possible. By sampling the FPD uniformly, we can recover the unobserved projections with high probability. The resulting optimal CA is called a "blue noise CA," since its distribution exhibits the spatial characteristics of the blue noise patterns, which suppress low-frequency components of noise [18,19]. Intuitively, blue-noise sampling generates randomized uniform point distributions, conversely to random patterns, where samples can be close or far from each other. In Section 4A, the PSNR of the estimated measurements at the FPD is presented for the proposed optimized CAs, alternative designs, and random CAs.
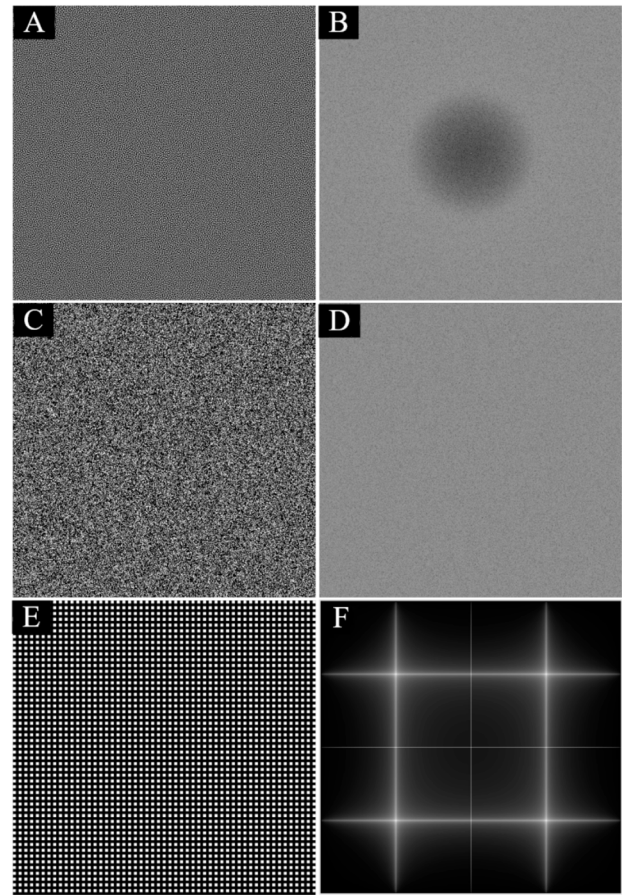

Fig. 2. (A) DBS Blue noise CA and (B) its 2D Fourier spectrum. (C) Random CA and (D) its 2D Fourier spectrum. (E) Bayer CA and (F) its 2D Fourier spectrum.

To find the optimal blue noise patterns for the CAs to be used in the cone-beam CT system, we used the direct binary search (DBS) algorithm. DBS was originally developed in halftoning to optimally represent continuous-tone images [20]. It is an iterative approach that evaluates the effect of trial changes for each pixel in a binary image until it closely resembles the original image after low-pass filtering. Here, the original image corresponds to a single intensity image with a gray-level equal to the CA's desired transmittance, and, due to its resemblance to the human visual perception, an exponential model is used as the low-pass filter [19]. The algorithm starts with a random CA of the target transmittance. Then, at each pixel location, the effect of toggling the pixel's state or swapping its value with any of its eight nearest neighbors is evaluated. The operation that results in the lowest difference to the original image is performed; then, the algorithm moves to the next pixel. Figure 2(A) depicts the first 102×105 pixels of a single realization of a blue noise CA obtained using the proposed DBS algorithm for a 614×630 detector and 25% transmittance. The size of the detector is derived from the testbed used in this manuscript, as shown in Section 4. Note, the Fourier spectrum shown in Fig. 2(B) has weak low-frequency energy but strong high-frequency energy, which results in a uniform distribution of the blocking elements, as shown in Fig. 2(A). On the other hand, random CAs like the one depicted in Fig. 2(C) have a flat Fourier

spectrum (depicted in Fig. 2(D)) that contains an equal amount of energy in all frequency bands. Additionally, given the random spatial distribution of these codes, clusters of zero-valued elements are likely to appear, as shown in Fig. 2(C). Finally, note that it is also possible to obtain a uniform structure using a Bayer pattern as shown in Fig. 2(E), which pushes the energy to higher frequencies, but on a regular pattern as shown in Fig. 2(F) [21]. This CA, however, gives less flexibility if modifications are needed when manufacturing the CA as the structure of the Bayer pattern is always similar to a checkerboard, as shown in 2(E). In the latter case, if the structure changes then the uniformity can be lost. With the DBS algorithm, on the other hand, one can add modifications to the patterns while attaining uniformity given that multiple blue noise patterns obey the uniformity constraint embedded in the algorithm. Note the frequency of the blue noise pattern of the CA determines the percentage of rays that are blocked at each view angle. In this experiment, we selected 25%, as this ideally reduces 75% of the radiation, which is a common goal for state-of-the-art X-ray radiation dosage reduction methods.

4. MATERIALS AND METHODS

We used the Rigaku GX 130 CT Scanner located in the Advanced Material Characterization Laboratory (AMCL) at the University of Delaware to obtain the X-ray projection data. Due to hardware constraints, the mounting hardware for CAs on the Rigaku CT scanner is located on the detector side as shown in Fig. 3(A). However, it can be shown that the forward model of the system does not change if the CA is placed after the object and before the detector. In this work, micro-CT projection data of a *Juglans hopeiensis* walnut were obtained at $P = 803$ view angles uniformly distributed around the object. This number of projections is suggested by the configurations of the scanner, and we refer to it as the "full-set" of projections. Table 1 has the remaining hardware settings used for the microCT scanner.

Table 1.   Hardware Settings Used for the Rigaku GX 130 CT

Setting	Value
X-ray focus (min)	5 μm
X-ray source to center of rotation	120 mm
FPD to center of rotation	224 mm
X-ray tube potential	130 kV
X-ray tube current	61 μA
Al filter	5 mm
Cu filter	0.06 mm
FPD size	2352 × 2944 pixels
FPD detector elements' size	49.5 μm

A. Simulation Results

In this work, we extract the bounding box of the walnut projections, which corresponds to the center 1842×1890 region of the FPD. The FDK cone-beam reconstruction algorithm from the ASTRA tomography toolbox [22] was used to reconstruct the $512 \times 512 \times 512$ FDK-reference volume of the walnut with a voxel size of 90 μm. In this paper, we use cubic voxels, but the proposed algorithm can be generalized to other geometries by making the appropriate adjustments in the CT reconstruction stage. We used the full set of projections without pixel binning for the reconstruction of the reference volume. In contrast, our previous work in [3] used binned projections to reconstruct the reference volume. Figure 3(B) shows the principal slice directions on the reference volume; Fig. 3(C) depicts its central axial slice. We evaluate the reconstruction quality by comparing the reconstructed object in each case to the reference FDK volume [23]. Particularly, we used the PSNR, calculated as $\text{PSNR} = 10\log_{10}(R^2/\text{MSE})$, where R is the maximum value in the reference data cube, and the MSE of two N^3 data cubes, I_1 and I_2, is $\text{MSE} = \sum_{x,y,z}[I_1(x, y, z) - I_2(x, y, z)]^2/(N^3)$, and the structural similarity index (SSIM). Finally, it should be noted that the radiation dosage in all the low-dose systems compared in this subsection is set to be equivalent for a fair comparison.
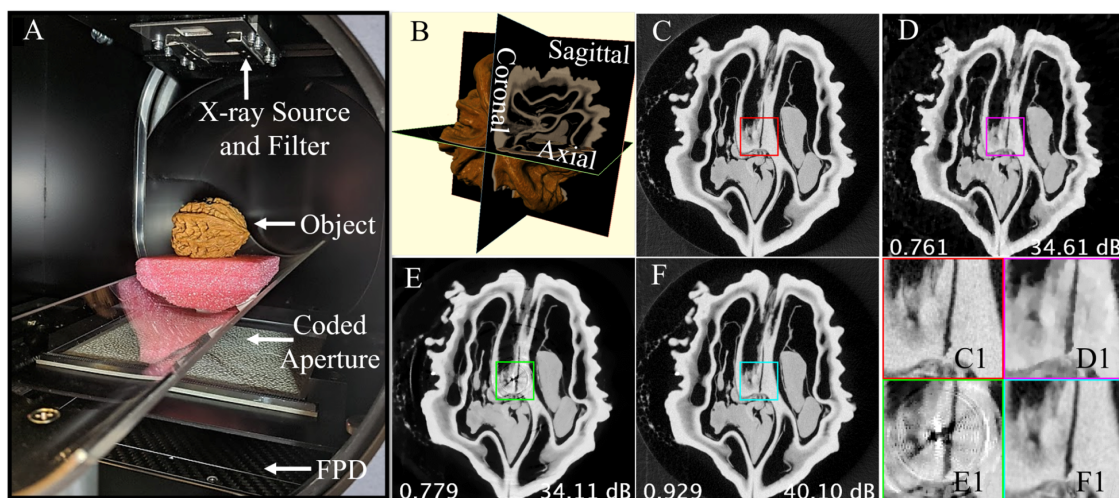

Fig. 3.   (A) Rigaku GX 130 CT Scanner with CA mounting hardware. (B) Principal slice directions of a *Juglans hopeiensis* walnut. Central axial slice reconstructions for (C) conventional CT and FDK algorithm. CS-based algorithms and (D) SparseCT, and (E) StaticCodeCT with an optimized CA. (F) Proposed approach. (C1)–(F1) Zoom of the highlighted regions. Depicted PSNR and SSIM were calculated per slice.

The first simulation experiment compares the StaticCodeCT system using an optimized CA with the SparseCT system [24,25]. For both systems, we used the CT configuration as shown in Table 1. Due to hardware constraints for the GPU implementation of the tensor completion algorithm used for the measurement estimation, we performed pixel binning to attain 614×630 projections, that is, the effective pixel size at the detector was set to 148.5 um. In this subsection, the collimators' pixel elements, and the CA elements are designed to have a one-to-one correspondence with the detector. For the SparseCT system, we used the same configuration described in [3], and 3D-TV regularization was used for the reconstruction [26]. Figure 3(D) depicts the central axial slice of the SparseCT reconstruction. The volume PSNR and SSIM attained with SparseCT were 38.22 dBs and 0.8, respectively. For the StaticCodeCT system, an optimized CA with 25% transmittance is emulated by setting to zero the FPD measurements that correspond with the location of the blocked elements on the CA at each view angle. Figure 3(E) depicts the reconstructed slices obtained using 3D-TV regularization and the algorithm in [26] using the observed measurements only. Note that we obtained the same behavior described in [3]; however, with the optimized CA, the rings describe a more uniform structure, as shown in Fig. 3(E-1). The results attained with the algorithm proposed in [3] have a volume PSNR and SSIM of 43.12 dBs and 0.96, respectively. Figure 3(F) depicts the reconstruction obtained using the FDK algorithm after the proposed tensor completion is performed to recover the missing projection data. The volume PSNR of the reconstruction obtained using the proposed method is approximately 5 dBs higher than the PSNR obtained using conventional CS algorithms and the SparseCT systems.

We performed a second experiment to compare the performance of the StaticCodeCT system to the sparse view-angle CT system because the latter is the state-of-the-art preferred standard to reduce the number of measurements in X-ray imaging systems [27]. The reconstruction algorithm used to reconstruct the object in the sparse view-angle CT system is the 3D TV regularization algorithm developed in [26]. The cone-beam hardware configuration remains unchanged from the previous experiment. Two CA CT systems with 25% transmittance are emulated. Then, the resulting coded projections are inpainted using the algorithm described in [3]. The first CA had a blue noise pattern obtained using the algorithm described in Section 3, while the second CA had a random pattern. Figure 2 depicts a 102×105 section of the 614×630 CAs and their corresponding spectra. Subsequently, we used the FDK reconstruction algorithm to recover the data cube in all cases. Figures 4(A)–4(C) depict the central 256th sagittal, coronal, and axial reference slices, respectively. Figures 4(D)–4(F) depict the reconstructions obtained using the optimized CAs with volume PSNR and SSIM of 43.12 dBs and 0.96, respectively; Figs. 4(G)–4(I) depict the reconstructions obtained using the random CAs with volume PSNR and SSIM of 42.13 dBs and 0.95, respectively; Figs. 4(J)–4(L) depict the reconstructions obtained using sparse view angles with volume PSNR and SSIM of 38.48 dBs and 0.87, respectively. For a fair comparison, the available view angles are uniformly sampled to obtain $P = 201$ for the sparse view-angle CT system. Namely, the resulting 201
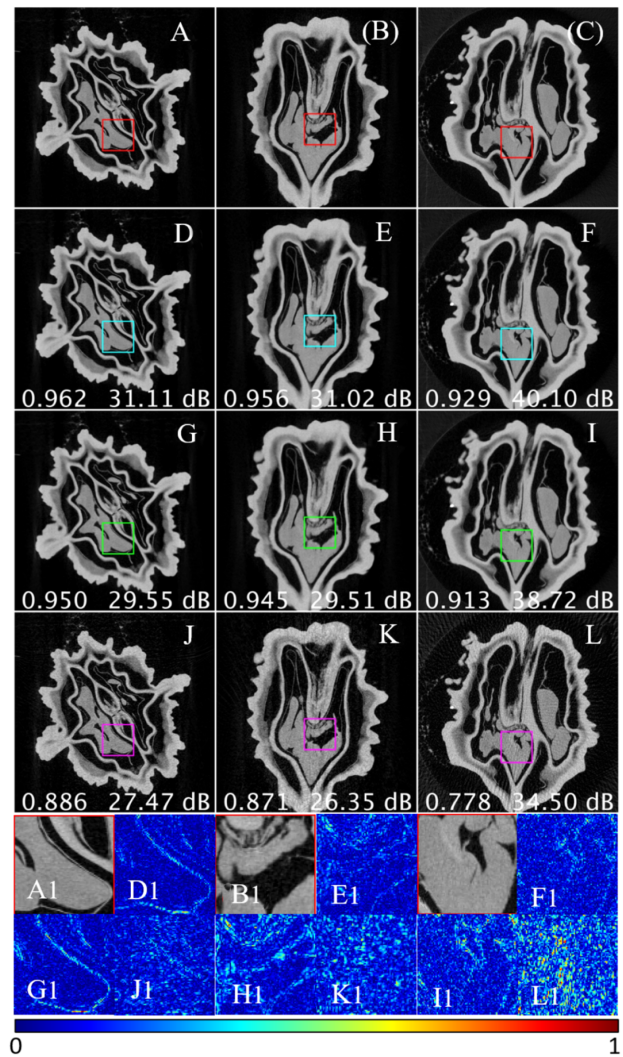

Fig. 4. FDK Reconstructions of the central 256th sagittal, coronal, and axial slices of a *Juglans hopeiensis* walnut for (A)–(C) conventional CT, StaticCodeCT with 25% transmittance using a (D)–(F) blue-noise CA, and a (G)–(I) random CA. (J)–(L) Sparse view-angle CT. (A1)–(C1) Zoom of highlighted regions in (A)–(C). (D1)–(L1) Normalized absolute error of the highlighted regions in (D)–(L). Depicted PSNR and SSIM were calculated per slice.

angles are evenly distributed in the gantry orbit. We do not sample the view angles randomly given that it has been previously shown that uniformly sampling the view angles results in similar reconstruction quality compared with randomly sampling them [2]. The absolute error images of the highlighted regions, depicted in Figs. 4(A-1)–4(L-1), show that the proposed system can obtain smooth reconstructions using conventional and fast CT algorithms. Furthermore, the volume PSNR of the reconstructions obtained using the proposed approach is 5 dBs higher than that attained with the sparse-view CT system, and 1 dB higher than the PSNR of the reconstructions obtained using a random CA.

In the previous experiments, we assumed a one-to-one correspondence of the CA elements with the detector elements; in practice, however, this is a challenging task due to manufacturing restrictions. To evaluate the performance of the proposed
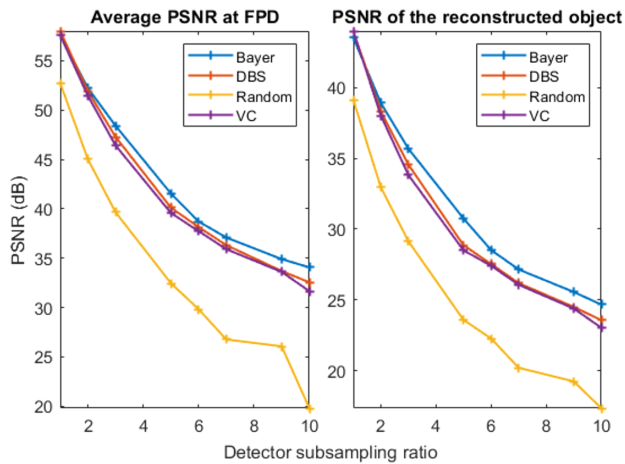
Fig. 5. Average PSNR obtained using DBS, void and cluster (VC), random, and Bayer CA for different mapping scenarios. Subsampling ratio of 10 corresponds to having a CA element map to 10×10 detector elements in the FPD.

optimized CAs as well as the reconstruction algorithm proposed in [3], we simulated a third scenario where the elements of the CA do not have a one-to-one correspondence with the detector elements. We maintained the same hardware CT configuration, but the pixel binning was modified to attain 630×630 projections on the center 1890×1890 region of the FPD. For this analysis, we compared both the PSNR of the tensor of measurements and the PSNR of the reconstructions obtained in each case. Additionally, given that multiple algorithms produce a uniform distribution of elements in the CA, we evaluate the performance of three different strategies: (A) DBS algorithm described in Section 3; (B) void and cluster algorithm [19]; and (C) Bayer patterns. We compare these three strategies with random CA when the CA elements map to 1×1, 2×2, 3×3, 5×5, 6×6, 7×7, 9×9, and 10×10 pixels on the detector. For all the CA, the transmittance was approximately 25%. Figure 5 depicts the average PSNR obtained in the measurement domain and the volume PSNR of the reconstructed object for each case. When there is one-to-one correspondence, the DBS algorithm gives the highest performance. Note the uniform CAs have higher performance than the random CA, and the three strategies only differ in 1 to 2 dBs for a different number of pixels at the detector. For the next section, we selected the DBS algorithm because this algorithm allowed for modifications needed for the CA manufacturing.

B. CA Manufacturing

Additive manufacturing (AM) is a rapidly evolving technology used to fabricate geometrically complex structures using a layer-by-layer material deposition process. In this work, three different AM techniques to build the CAs were investigated.

1. Metal CA

Wolfmet 3D is a metal additive manufacturing (MAM) process provided by M&I Materials [10]. It uses a high-power laser to fuse and melt specific parts of successive layers of metallic powders to build 3D structures, a technique called "selective laser melting." For the CA used in this work, the metallic powder is pure tungsten. Objects fabricated using this technique can be mechanically weak and do not have a self-supporting structure. Namely, if there is a blocking element surrounded by "unblocking elements," then this element would be floating as the CA frame would not support it. The thickness is set to be 2 mm to avoid a fragile structure and prevent damage during the EDM wire-cutting process, in which the part is separated from a steel back-plate used for construction. Additionally, the CA must be self-supporting, i.e., a structure with no two holes touching (NTHT). However, the DBS algorithm used to attain the blue noise patterns, which are optimal for the StaticCodeCT system, does not necessarily produce an NTHT distribution. Thus, the algorithm used to attain the MAM CA alternates between blue noise generation using DBS and the removal of blocking elements inside clusters of unblocking elements until there are no more possible changes, and a self-supporting structure is obtained. Hereinafter, this CA will be referred to as MAM (depicted in Fig. 6(A)).

2. Plastic CA

Cold casting is a low-cost AM method that casts a radiopaque material onto a 3D printed structure. Given the support of the mold the pattern does not need to be NTHT, and the CA elements' dimensions can be adjusted for different applications. In this work, the radiopaque material is a tungsten epoxy resin composite (Technon Poly Kits [28]), which contains 100 mesh tungsten powder (149 µm maximum particle size) and two-part epoxy resin. According to the mixing instructions for Poly/Technon, the required compound viscosity (ρ) ranges from 9.5 to 10.5 gr/cc, and the maximum percentage of powder that can be mixed with the resin composite is 96.2% by weight. Thus, for a pourable compound, this ratio was maintained below 93.5%. Two plastic mold designs were sent to Shapeways [29] for manufacturing. The printing material was set to "Fine Detail Plastic" with two printing options, smooth and smoothest, with resolutions of 32 µm and 29 µm for CAs with pixel pitch 576 and 493 µm, hereinafter referred to as CC576 and CC493, respectively. Figure 6(B-1) depicts the 3D printed plastic mold; Fig. 6(B-2) depicts the result after casting the tungsten-epoxy mixture. This structure was cured for 24 h at room temperature and then polished [11]. Figure 6(C) depicts the polished result for the CC576 CA.

3. Ceramic CA

Ceramic-based additive manufacturing offers advantages over traditional manufacturing processes that require high mechanical strength and thermal resilience. Conventional manufacturing of ceramics is a time-consuming and expensive process that is often limited in geometrical complexity, where these limitations are often amplified when producing high-resolution features. In this work, yttria-stabilized zirconia ceramic parts were fabricated using the XJet Carmel 1400 system. This AM system utilizes a proprietary nanoparticle jetting technology (NPJ) that deposits small droplets of ink consisting of a highly loaded dispersion of ZrO_2 nanoparticles (>10 nm) suspended within a carrier-agent or support
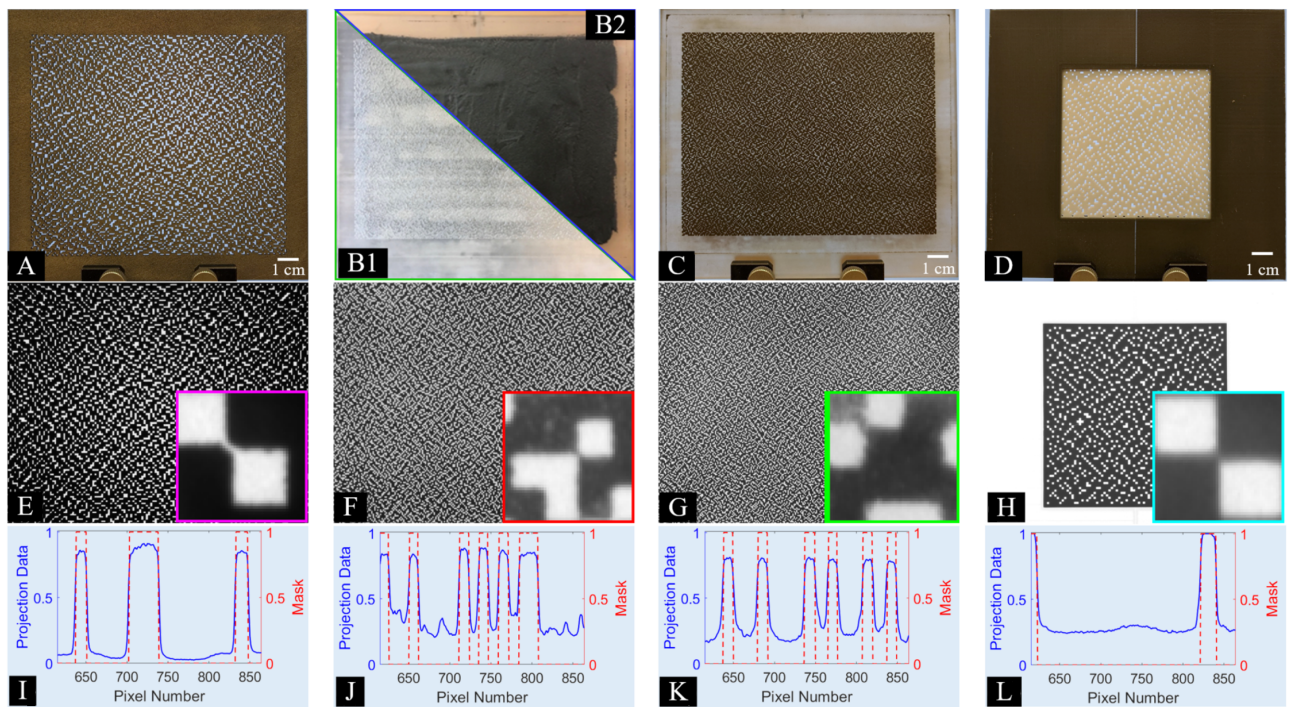
Fig. 6. (A)–(D) Coded aperture photos, bottom white line indicates the scale, (E)–(H) transmission radiographs, (I)–(L) horizontal line profiles in the transmission radiograph. Left to right, the columns correspond to MAM, CC493, CC576, and ceramic CAs. (B1) 3D printed plastic mold. (B2) Poly/Technon cast into the plastic mold.

material inks. During the printing process, and after the print carriage completes a material deposition pass, heating lamps and a hot air dryer evaporate the carrier agent from the top surface. Afterward, an abrading roller planarizes the print surface before the next material print pass. This process consolidates the material and smooths the surface for subsequent layers, where these processes are repeated layer-upon-layer until the full 3D part is completed. After the print process has finished, the build tray is submerged within a circulating water bath at 30°C to initiate the dissolution of support material. The removal of support material can take as long as 24 h depending on the size and complexity of the printed part. After the support material has been completely removed, the part is carefully placed into a desiccating chamber and allowed to dry completely. Last, the fully dried green ceramic parts are fired in a sintering furnace using a programmable heating profile, up to nearly 48 h. After reaching temperatures of 1450°C, the ceramic nanoparticles sinter together, forming an isotropic part that reaches 99.5% theoretical density. An example of a CA with a thickness of 0.73 mm obtained using this process is shown in Fig. 6(D).

The number of elements in each CA was determined by the manufacturing constraints of each method. In all cases, the CA elements mapped to more than one detector element on the FPD. Furthermore, the CA holder in the Rigaku CT scanner allowed for the placement of a 5 mm thick structure that was not adjustable. Thus, for each CA, different arrangements were needed for the CA placement. In the MAM case, a 3 mm thick plastic frame was 3D printed and placed together with the MAM CA in the holder, which allowed the CA to be as close to the detector as possible. On the other hand, given the flexibility in the CC576 and CC493 structures, the thickness

of the area of the CAs aligned with the mounting frame was calculated to minimize the number of detector elements corresponding to a projection of a single CA element. Last, in the ceramic case, given the reduced size of the CA, a frame that could hold the structure in the middle, for stability purposes, was 3D printed and can be seen around the CA in Fig. 6(D). The pixel pitch, thickness, approximate number of detector pixels on the detector (DPD), and distance from the detector (DD) for each of the CAs can be found in Table 2. The latter is measured from the center of the detector to the center of each structure. Figures 6(E)–6(H) depict the transmission radiographs measured in the Rigaku CT scanner for each CA at s_1. An enlarged area highlighted in each CA shows defects proper of each manufacturing method. The MAM CA has the highest density and thickness; thus, it has the greatest attenuation. However, it presents rounded corners due to the resolution of the 3D printing process and the thickness of the CA as shown in Fig. 6(E). Figures 6(C) and 6(D) correspond to the cold-cast CAs (CC493 and CC576), which present voids due to air trapped in locations that should be radiopaque. Figure 6(G) corresponds to the ceramic CA, which covers a smaller area due to manufacturing constraints; however, similar to the MAM CA, it has a more uniform projection given the uniformity of the 3D printed material. Note, only the CA elements of the cold-cast CAs are cubic. In all the other cases, due to manufacturing constraints, the thickness and the pixel pitch of the CA elements are different. This disparity leads to having varying projection sizes of a CA element on the detector, especially close to the borders of the FPD.

Ideally, X-rays should originate from a point source. However, this is not the case in real implementations, which

Table 2.   CA Dimensions

Code	Pitch (μm)	Thickness (μm)	DPD	DD (mm)
MAM	900	2000	22	38.00
CC493	493	493	12	38.09
CC576	576	576	14	37.82
Ceramic	940	730	17	39.5

present a "geometric" penumbra effect governed by the size and shape of the X-ray focal spot. Furthermore, when a CA is placed in front of the X-ray source, X-rays will pass through the edges of the unblocked elements of the CA resulting in "transmission penumbra." The size of this penumbra will increase with the thickness and pitch size of the CA elements, and the size of the "geometric" penumbra will decrease as the CA is placed farther from the X-ray source. To deal with these effects, object-free projections using each mask are obtained with the CT scanner. Then, using thresholding-based image segmentation, a mask array indicating the location of the measurements free from errors is obtained [25]. Figures 6(I)–6(L) depict a line profile across the detector bins at the 780th row for each CA normalized projection. Note, the unblocked elements are closer to 1 for the ceramic and MAM Cas, as there is not any material on the X-ray path in these cases. In the cold-cast CAs, on the other hand, the fluctuations in the line profiles suggest there is leakage of radiopaque material into the translucent elements, caused by errors at the moment of polishing. These CAs, however, achieve the best reconstruction quality compared with the MAM and ceramic CAs. The binary mask obtained by thresholding the normalized measurements is depicted in a red dotted line for each case. The larger the thickness and pixel pitch, the more data are unused after applying the mask. All CA patterns had 30% transmittance at the time of fabrication. After the binary mask is applied, the number of measurements used for the estimation for the MAM, CC493, CC576, and ceramic CAs are 21.09%, 24.50%, 25.67%, and 14.81%, respectively.

CAs filter the X-ray spectra depending on the thickness and density of the material used in the blocking elements. In this work, the Amptek X-123CdTe X-ray spectrometer was used to measure the filtered X-ray spectrum in each case and thus determine the percentage of energy blocked by each CA. For this experiment, an X-ray microfocus source with a tungsten target was operated at 130 kV and 3 μA. The spectrometer measured 1024 energy channels and a tungsten collimator was used to reduce the incoming X-ray flux and avoid saturation. The distances from the source to the CA and the spectrometer were set to 100 and 800 mm, respectively. Figure 7 depicts the X-ray source spectrum and the filtered spectra for each CA. The energy is calculated from 30 to 130 keV, for each case. As expected, the MAM CA blocks more than 99% of the original X-ray spectrum. The CC493 CA, on the other hand, only blocks 86% of the energy, given the thickness of the radiopaque material. Last, the CC576 and the ceramic CAs block approximately 97% of the energy. The latter demonstrates that the ceramic CAs can be used as a radiopaque material to block the X-rays.

C. Experimental Results

The four CAs specified in Table 2 are placed in the Rigaku CT lab, and the previous cone-beam configuration is used to attain
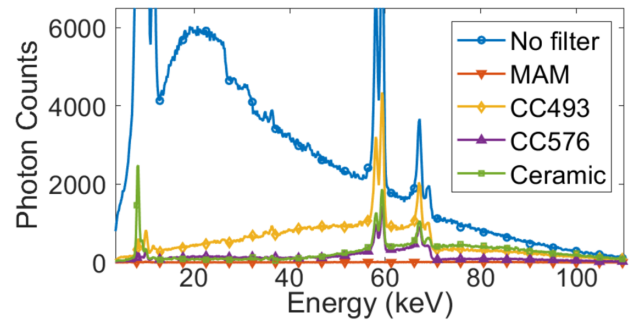

Fig. 7.   Measured X-ray spectra of a 130 kV X-ray source with a tungsten target using the blocking elements of each CA.

$P = 803$ projection measurements of a *Juglans hopeiensis* walnut. Due to hardware constraints for the GPU implementation of the tensor completion algorithm used for the measurement estimation, the FPD measurements obtained with the MAM, CC493, and CC576 CAs are cropped to an area of 1842×1890 pixels; then, they are binned to a 614×630. In the ceramic case, the projections are cropped to a smaller region given the dimensions of the CA. Namely, an area of 1560×1764 pixels on the detector is cropped; then, after pixel binning, a 520×588 measurement is obtained per view angle. In all cases, the detector pixel pitch after binning corresponds to 148.5 μm. The PSNR and SSIM in the slices are calculated in the circle of radius N containing the walnut.

The coded projections are first inpainted using the matrix completion algorithm to attain a suitable initialization. Then, the estimated FPD measurements are stacked vertically, and the tensor completion framework is used to estimate the measurement's tensor. The reconstructions of the central 257th axial slice of the walnut obtained with each CA using the proposed measurement's estimation approach with the FDK, and the simultaneous iterative reconstruction technique (SIRT) algorithms are depicted in Figs. 8(A)–8(D) and Figs. 8(E)–8(H), respectively. Given the higher number of elements used for estimation in the cold-cast CAs' case, the reconstructions obtained using the CC493 and CC576 CAs have a higher PSNR and SSIM, compared with the reconstructions obtained using the CAs attained using the MAM and ceramic CAs. Furthermore, the resulting effective detector pitch in each case determines the resolution that can be attained for each experiment; in [3], the authors demonstrate how the proposed method changes the MTF of the system. The ceramic CAs have the lowest reconstruction quality given the low number of elements used for the measurement estimation explained due to a bend on the structure obtained after curing the sample. However, this manufacturing method has the potential of obtaining high resolution with a small thickness, and techniques to address the manufacturing drawbacks are currently being studied. Additionally, note the CC493 reconstructions have higher PSNR and SSIM than the CC576 reconstructions. This effect is expected because the area of the projected CA elements of the CC493 CA is smaller. Thus, the proposed estimation algorithm performs better in this case.

For comparison, a CS-based reconstruction algorithm, specifically the 3D TV regularization algorithm developed in [26], is used to iteratively solve Eq. (3) for the observed
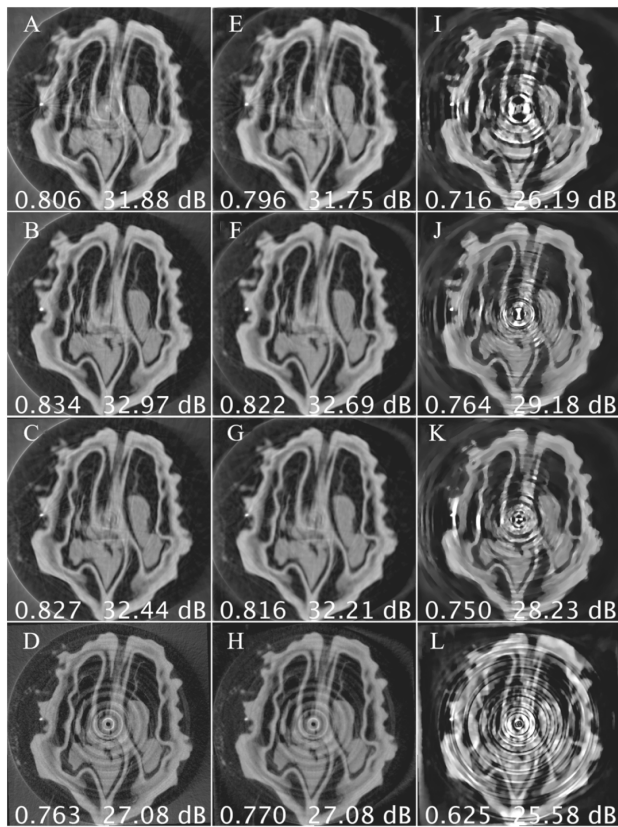
Fig. 8. Central 257th axial reconstructions using the proposed approach with the (A)–(D) FDK, and (E)–(H) SIRT algorithms. (I)–(L) CS-based algorithms for MAM, CC493, CC576, and ceramic CAs, respectively. Depicted PSNR and SSIM are calculated per slice.

measurements. Figures 8(I)–8(L) depict the central axial slice reconstruction for each CA. The reconstructions show concentric ring artifacts associated with the position of the
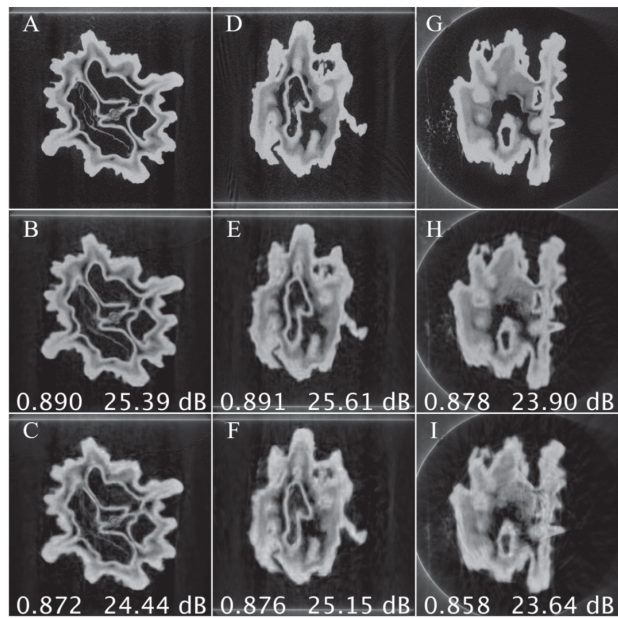

Fig. 9. 128th Sagittal, coronal, and axial reconstructions. (A)–(C) Reference. Proposed method using (D)–(F) MAM, and (G)–(I) CC493 CAs. Depicted PSNR and SSIM were calculated per slice.

blocking elements of the CAs. Interestingly, these artifacts are visually similar to the SD distribution of the static CA system. Additionally, note the PSNR of the reconstructions obtained using the proposed approach is approximately 3 dB higher than the PSNR of the CS reconstructions and the SSIM is superior for all the CA experiments. To further compare the 3D reconstructions of the two manufacturing methods with the highest performance as well as to demonstrate that the 3D volume reconstruction is available, Fig. 9 depicts the 128th sagittal, coronal, and axial slices reconstructed using the proposed method for the MAM and the CC493 CAs. Note the ring artifacts in the reconstruction are less pronounced, and the PSNR and SSIM for both CAs are higher compared with the central slices.

5. CONCLUSIONS AND FUTURE WORK

The feasibility of using a single CA mask in a coded aperture CT system was experimentally demonstrated using a cone-beam X-ray microtomography system. Unlike previous approaches to coded aperture CT based on the CS theory, we used our previously introduced reconstruction framework based on the completion of a 3D low-rank tensor in the measurement domain. Additionally, even though a systemic approach to designing an optimum sampling scheme is not straightforward, the matrix completion scheme used for measurement estimation was leveraged to produce optimal codes with a blue-noise structure; further, their higher performance was demonstrated through simulations using real projection data.

Note that the reconstructions obtained using the emulated CAs present higher PSNR and SSIM than those that were attained using the real CAs. These can be explained by several factors: (I) the tensor completion framework is affected when the blocking elements do not correspond with the elements on the FPD because this would correspond as having clusters of unknowns in the tensor; (II) the CAs were designed to have a particular transmittance, but due to the correction for the geometric aberrations and the penumbra effect the resulting transmittance of the codes in the experimental section is much lower; (III) using the coded masks in front of the X-ray source presents a potential advantage because an efficient scatter estimation and correction can be applied and calculated with the prior information known of the mask [30].

The performance of the proposed reconstruction framework and the optimal codes was compared with state-of-the-art algorithms and alternative low-dose tomography systems using quantitative and qualitative measures. The proposed method was found to produce higher-quality reconstructions. Additionally, reconstruction results using real CAs show that the proposed algorithm leads to reconstructions with higher PSNR than the ones obtained using compressed sensing reconstruction algorithms when a single CA is used for all view angles. Note that, given hardware constraints in the micro-CT scanner, the mounting hardware for CAs on the testbed is located on the detector. As a result, the reconstructions presented in this paper suffer less from the penumbra effect compared with having the masks on the source side. However, the blocking effect is equivalent for testing the proposed single CA approach; the procedure described to account for the penumbra effect can be applied in these cases as well.

REFERENCES

1. J. Z. Liang, P. J. La Riviere, G. El Fakhri, S. J. Glick, and J. Siewerdsen, "Guest editorial low-dose CT: what has been done, and what challenges remain?" IEEE Trans. Med. Imag. **36**, 2409–2416 (2017).
2. Y. Kaganovsky, D. Li, A. Holmgren, H. Jeon, K. P. MacCabe, D. G. Politte, J. A. O'Sullivan, L. Carin, and D. J. Brady, "Compressed sampling strategies for tomography," J. Opt. Soc. Am. A **31**, 1369–1394 (2014).
3. A. P. Cuadros, X. Ma, C. M. Restrepo, and G. R. Arce, "StaticCodeCT: single coded aperture tensorial X-ray CT," Opt. Express **29**, 20558–20576 (2021).
4. A. P. Cuadros, C. Peitsch, H. Arguello, and G. R. Arce, "Coded aperture optimization for compressive X-ray tomosynthesis," Opt. Express **23**, 32788–32802 (2015).
5. T. Mao, A. P. Cuadros, X. Ma, W. He, Q. Chen, and G. R. Arce, "Fast optimization of coded apertures in X-ray computed tomography," Opt. Express **26**, 24461–24478 (2018).
6. T. Mao, A. P. Cuadros, X. Ma, W. He, Q. Chen, and G. R. Arce, "Coded aperture optimization in X-ray tomography via sparse principal component analysis," IEEE Trans. Comput. Imag. **6**, 73–86 (2020).
7. A. P. Cuadros and G. R. Arce, "Coded aperture optimization in compressive X-ray tomography: a gradient descent approach," Opt. Express **25**, 23833–23849 (2017).
8. A. Parada-Mayorga, A. Cuadros, and G. R. Arce, "Coded aperture design for compressive X-ray tomosynthesis via coherence analysis," in *IEEE 14th International Symposium on Biomedical Imaging (ISBI)* (2017), pp. 44–47.
9. A. Holmgren, "Coding strategies for X-ray tomography," Ph.D. thesis (Duke University, 2016).
10. M&I Materials, "Innovation for personalised cancer treatment with Wolfmet 3D Tungsten collimator and depict project," www.wolfmet.com/wp-content/uploads/2017/07/Wolfmet-3D-and-DEPICT-Case-Study-Aug.pdf.
11. A. A. M. Muñoz, A. Vella, M. J. F. Healy, D. W. Lane, I. Jupp, and D. Lockley, "Rapid prototyping-coded masks for X-ray backscatter imaging," Opt. Eng. **57**, 085104 (2018).
12. P. Parsons, Z. Larimore, A. Good, A. Clark, S. Gatley, J. Federici, and M. Mirotznik, "Millimeter and sub-millimeter wave electromagnetic characterization of additively manufactured zirconia ceramics via nanoparticle jetting," in IEEE Transactions on Components, Packaging and Manufacturing Technology (2020).
13. J. Prince and J. Links, *Medical Imaging Signals and Systems* (Pearson Prentice Hall, 2006).
14. K. Choi and D. Brady, "Coded aperture computed tomography," Proc. SPIE **7468**, 74680B (2009).
15. H. Arguello and G. R. Arce, "Colored coded aperture design by concentration of measure in compressive spectral imaging," IEEE Trans. Image Process. **23**, 1896–1908 (2014).
16. E. J. Candes and B. Recht, "Exact low-rank matrix completion via convex optimization," in *46th Allerton Conference on Communication, Control, and Computing* (2008), pp. 806–812.
17. D. L. Pimentel-Alarcon, N. Boston, and R. D. Nowak, "A characterization of deterministic sampling patterns for low-rank matrix completion," IEEE J. Sel. Top. Signal Process. **10**, 623–636 (2016).
18. D. L. Lau, R. Ulichney, and G. R. Arce, "Blue and green noise halftoning models," IEEE Signal Process. Mag. **20**(4), 28–38 (2003).
19. D. L. Lau and G. R. Arce, *Modern Digital Halftoning*, 2nd ed. (CRC Press, 2007).
20. J. P. Allebach, "DBS: retrospective and future directions," Proc. SPIE **4300**, 358–376 (2000).
21. T. Rao, G. Arce, and J. Allebach, "Analysis of ordered dither for arbitrary sampling lattices and screen periodicities," IEEE Trans. Acoust. Speech Signal Process. **38**, 1981–2000 (1990).
22. W. van Aarle, W. J. Palenstijn, J. Cant, E. Janssens, F. Bleichrodt, A. Dabravolski, J. D. Beenhouwer, K. J. Batenburg, and J. Sijbers, "Fast and flexible X-ray tomography using the Astra toolbox," Opt. Express **24**, 25129–25147 (2016).
23. J. Bian, J. H. Siewerdsen, X. Han, E. Y. Sidky, J. L. Prince, C. A. Pelizzari, and X. Pan, "Evaluation of sparse-view reconstruction from flat-panel-detector cone-beam CT," Phys. Med. Biol. **55**, 6575–6599 (2010).
24. M. J. Muckley, B. Chen, T. Vahle, T. O'Donnell, F. Knoll, A. D. Sodickson, D. K. Sodickson, and R. Otazo, "Image reconstruction for interrupted-beam X-ray CT on diagnostic clinical scanners," Phys. Med. Biol. **64**, 155007 (2019).
25. T. Lee, C. Lee, J. Baek, and S. Cho, "Moving beam-blocker-based low-dose cone-beam CT," IEEE Trans. Nucl. Sci. **63**, 2540–2549 (2016).
26. T. Jensen, J. Jørgensen, P. Hansen, and S. Jensen, "Implementation of an optimal first-order method for strongly convex total variation regularization," BIT Numer. Math. **52**, 329–356 (2012).
27. J. S. Jorgensen, E. Y. Sidky, and X. Pan, "Quantifying admissible undersampling for sparsity-exploiting iterative image reconstruction in X-ray CT," IEEE Trans. Med. Imag. **32**, 460–473 (2013).
28. Tungsten Heavy Powder and Parts, "Technon poly kits," www.tungstenheavypowder.com/technon-poly-kits/.
29. Shapeways, www.shapeways.com.
30. L. Ren, F.-F. Yin, I. J. Chetty, D. A. Jaffray, and J.-Y. Jin, "Feasibility study of a synchronized-moving-grid (SMOG) system to improve image quality in cone-beam computed tomography (CBCT)," Med Phys. **39**, 5099–5110 (2012).
31. A. Cuadros, "Sparse sampling in x-ray computed tomography via spatial and spectral coded illumination," Ph.D. thesis (University of Delaware, 2020).